Journal of Molecular Structure 1254 (2022) 132375

Contents lists available at ScienceDirect

Journal of Molecular Structure

journal homepage: www.elsevier.com/locate/molstr

Synthesis, structural, vibrational, molecular docking and nonlinear optical studies of (E)-N′-(2,3-dimethoxybenzylidene)-4-fluorobenzohydrazide

Jeeva P[a], Barathi D[a,*], Rajaboopathi Mani[b,c], David Stephen A[d], Marjatta Louhi-Kultanen[b], Vinitha G[e], Abdullah G. Al-Sehemi[f]

[a] NKR Government Arts College for Women, Namakkal, 637 001, Tamil Nadu, India
[b] Department of Chemical and Metallurgical Engineering, School of Chemical Engineering, Aalto University, P.O. Box 16100, FI-00076, Aalto, Espoo, Finland
[c] Centre for Research and Development, Department of Physics, PRIST Deemed to be University, Vallam, Thanjavur, 613403, Tamil Nadu, India
[d] Department of Physics, PSG College of Arts and Science, Coimbatore, 641014, Tamil Nadu, India
[e] Division of Physics, School of Advanced Sciences, Vellore Institute of Technology, Chennai, 600 127, Tamil Nadu, India
[f] Department of Chemistry, Faculty of Science, King Khalid University, Abha, 61413, P.O. Box 9004, Saudi Arabia

ARTICLE INFO

Article history:
Received 29 October 2021
Revised 4 January 2022
Accepted 7 January 2022
Available online 9 January 2022

Keywords:
Hydrazone
Crystallization
Density functional theory
Crystal structure
Vibrational analysis
Third harmonic generation

ABSTRACT

Organic nonlinear optical single crystals of (E)-N′-(2,3-dimethoxybenzylidene)-4-fluorobenzohydrazide (DMB-FBH) were synthesized and grown using slow evaporation crystallization from ethanol solution. The single crystal X-ray diffraction scattering revealed that the DMB-FBH crystallised in the tetragonal crystal system with a centro symmetric space group of I 4_1/a. The crystallographic bond lengths and bond angles were compared with the values generated from optimized molecular geometry based on quantum chemical calculations. The functional group vibrations were identified theoretically by density functional theory with B3LYP 6–311 G (d,p) basis set using Gaussian 09 software package and their vibrations were compared with the experimental FT-IR spectra. The UV-visible and the fluorescence emission spectra of the DMB-FBH in aqueous solutions were recorded. The HOMO-LUMO energy level pictogram addressed the intramolecular charge transfer (ICT) interaction between donor and acceptor moieties and their impact on the energy gap was determined. Different interactions such as O···H, N···H, C···C and C···H in DMB-FBH were quantified via fingerprint plots and these results were compared with that of similar structure. The detailed molecular docking simulation was carried out with M. tuberculosis protein [PDB ID:2 × 22]. The third order nonlinear optical susceptibility (χ^3) of DMB-FBH was confirmed experimentally by Z-scan method and their conversion efficiency was higher than the other hydrazones derivatives. In short, this work discusses the crystal structure, identification and quantification of the molecular interactions, thermal, antimycobacterial and optical properties of new hydrazone derivative.

1. Introduction

The non-linear optical (NLO) crystals are in high demand for light conversion applications as it requires for laser technology, optoelectronics, optical limiting, photonics and optical sensors [1–5]. The organic molecules over inorganics exhibit large NLO response owing to donor–acceptor groups with π-conjugated hydrogen bonding which enables high transfer of charge in the molecules [6]. The second and third order susceptibilities can confirm theoretically the conversion efficiency of molecules alongside experimental evidence [7]. The Kurtz-Perry powder or Makerfringes technique is considered as simplest and most accurate method to measure the NLO efficiency [8].

The synthesis of hydrazones (-NHN=CH-) has received attention due to its potential applications as anti-microbial, anti-flammatory and anti-cancer drugs [9]. In addition, the conjugated C=N bond with lone pair of electron in the nitrogen (nucleophilic) and their electrophilic and nucleophilic carbons made this compound applicable as precursors for organic and inorganic syntheses [10]. In general, the hydrazones are synthesized by reaction of hydrazide with carbonyl-containing compound, particularly aldehydes or ketones [11]. The crystallographic aspect of hydrazones derivatives has been discussed for few combinations and their inter and intramolecular hydrogen bonds influencing supramolecular arrays were studied [12]. For

* Corresponding author.
E-mail address: barathi.rammohan@gmail.com (B. D).

https://doi.org/10.1016/j.molstruc.2022.132375
0022-2860/

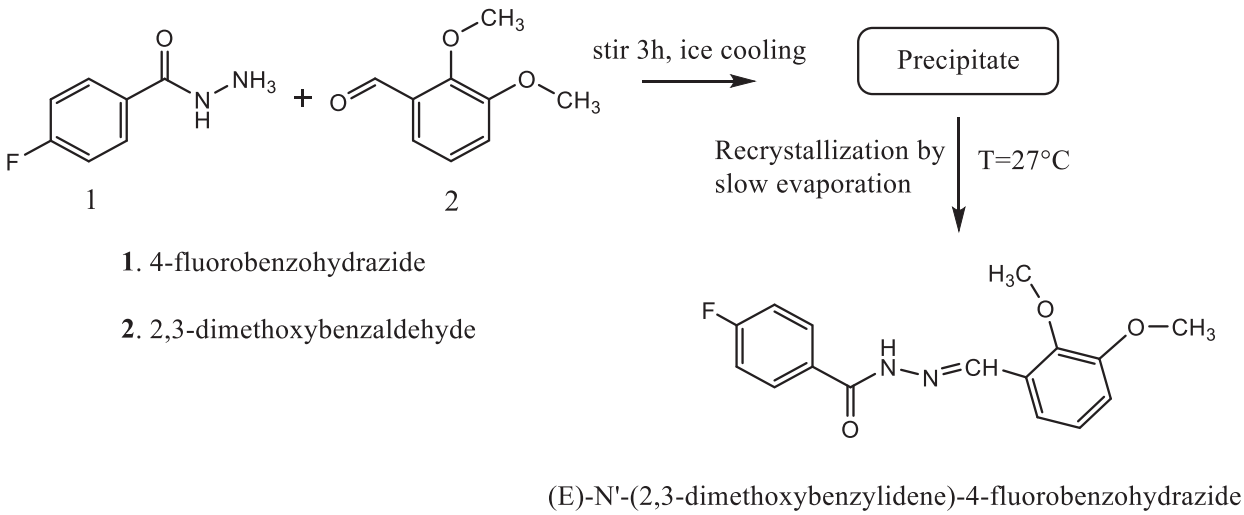

Scheme 1. Synthesis of Schiff base (E)-N′-(2,3-dimethoxybenzylidene)−4-fluorobenzohydrazide (DMB-FBH) crystals.

instances, the hydrazone formed from substituted benzaldehydes [13], and (pyrazinecarbonyl)hydrazones of substituted benzaldehydes [14] along with L-serinyl derivatives were reported. Furthermore, the synthesis and crystal structures of Schiff base (E)-N'-(3,4-dimethoxybenzylidene)furan-2-carbohydrazide and their intermolecular interactions have recently been discussed [11]. A weak intramolecular interaction has been realized in the gas phase due to monomeric form and it turns to strong in the solution due to loss of planarity in the molecular structure. Benzimidazole [15,16], benzofuran [17], xanthenone [18], xanthene [19] based hydrazone derivatives were synthesized for anti-bacterial and anti-diabetic applications as well as α-glucosidase inhibition, and nonlinear optical conversion. The nonlinear response to optical input has also been recorded in the Schiff base (E)-N′-(Benzo [d][1,3] Dioxol-5-ylmethylene) nicotinohydrazide monohydrate single crystals [20]. The fluorescence and absorption behaviours of substituted aryl hydrazones were reported [21]. On the industrial scale, the Schiff base hydrazides have wide range of applications such as dyes and pigments [22]. They have been used as chemical precursors, sensors and in catalytic processes [23–25].

This work discusses the synthesis of (E)-N′-(2,3-dimethoxybenzylidene)−4-fluorobenzohydrazide (DMB-FBH) by using the precursors 2,3-dimethoxy benzaldehyde and 4-fluorobenzohydrazide and their crystals growth and crystal structure. In addition, the detailed computational investigations of the structure, vibrational spectra, frontier molecular orbitals, and nonlinear susceptibility analyses have been discussed. We evaluated the antimycobacterial activity against M. tuberculosis [26] contains mycolic acids by targeting DMB-FBH on enzyme [Protein ID: 2 × 22] [27] via molecular docking simulation.

2. Experimental

2.1. Synthesis and crystallization of (E)-N′-(2,3-dimethoxybenzylidene)−4-fluorobenzohydrazide (DMB-FBH) compound

An ethanolic solution of 4-fluorobenzohydrazide (1.54 g, 0.01 M) was mixed with ethanolic solution of 2,3-dimethoxy benzaldehyde (1.66 g, 0.01 M) in a round-bottom flask. The solution mixture was put in the beaker and stirred on a magnetic stirrer with stir bar for 3 h. Then it was cooled down by poured into an ice-cold water mixture. The precipitates were formed and it was filtered out using Whatman filter paper and recrystallized by slow evaporation crystallization from ethanol solution at 27 °C. The colorless and transparent single crystals were observed in twenty days and it was used for further characterizations. The synthesis procedure is depicted in Scheme 1.

2.2. Characterizations

The single crystals X-ray diffraction data of DMB-FBH was collected using Bruker Smart APEX-II CCD diffractometer using Mo Kα radiation (λ = 0.71073 Å) with a graphite monochromator in the incident beam. Data were reduced using SAINT/XPREP software (Bruker, 2004). All of the non-hydrogen atoms were found using a direct-method analysis in the SHELX-97 software [28]. After several cycles of refinement, the positions of the hydrogen atoms were calculated and added to the refinement process. The vibrational spectra were recorded using a PerkinElmer FT-IR spectrophotometer in the region of 4000–400 cm^{-1} at KBr phase with the resolution of 1 cm^{-1}. The UV–Vis transmittance spectrum of DMB-FBH was recorded using PerkinElmer-spectrophotometer in the range of 800–200 nm. The fluorescence emission spectrum of DMB-FBH was recorded using PerkinElmer in the region 200–900 nm. These optical studies were performed in aqueous solution of DMB-FBH crystals. The third-order nonlinear refractive index (n_2) and nonlinear absorption coefficient (β) of DMB-FBH in ethanol were performed by closed and open aperture Z-scan techniques using a 532 nm CW DPSS Laser (Coherent Compass TM 215 M-50) with an input intensity of 100 mW. The peak intensity (I_0) at the focus was 8.36 kW/cm^2 and the Gaussian laser beam profile was focused to a waist (ω_0) of 12.5 µm. The sample was focused with maximum intensity with a focal length of 10.3 cm.

2.3. Computational details

The density functional theory quantum chemical calculation was performed by Gaussian 09 software package [29]. The crystallographic information file (.cif) generated from single crystal data of DMB-FBH was used as an input for the generation of initial geometry. The geometry optimizations were carried out in a gas phase by B3LYP level of theory with 6–311 G (d,p) basis set. The ground state structure was confirmed by frequency analysis and we have not observed any imaginary frequency. The HOMO-LUMO, FT-IR and NLO analyses of the DMB-FBH were also calculated. The UV–Vis analysis was computed employing time-dependent density functional theory (TD-DFT). The input files and the interpretation

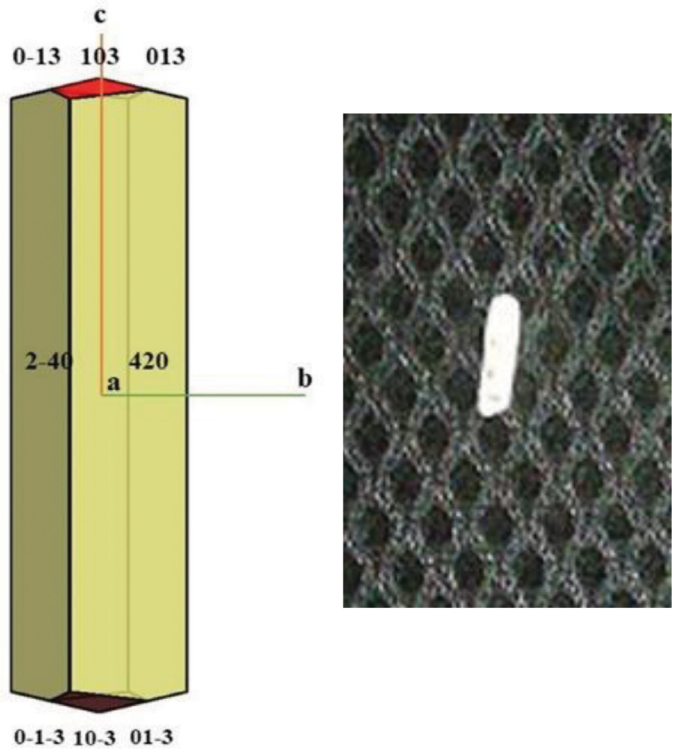

Fig. 1. Theoretically generated crystal morphology (left) and experimental grown crystal (right) of DMB-FBH.

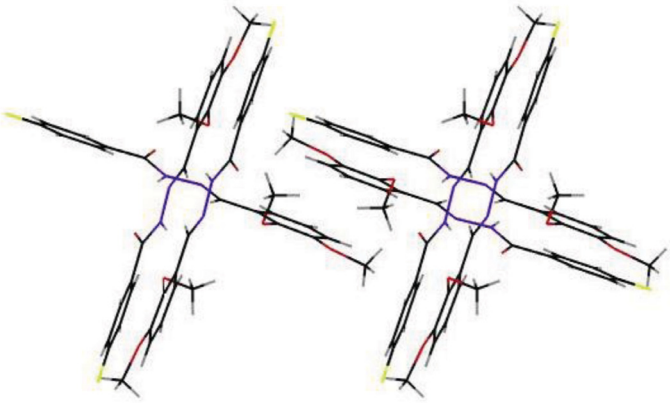

Fig. 2. Inter and intramolecular interactions of DMB-FBH crystals.

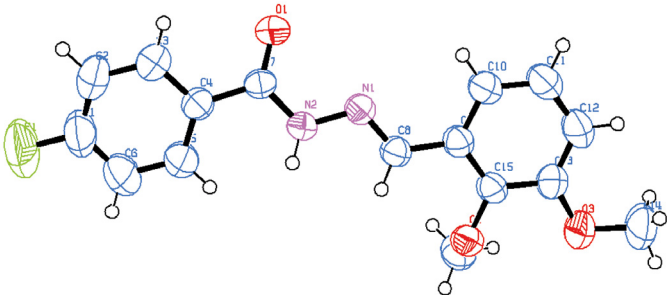

Fig. 3. The ORTEP diagram (50% probability level) of the DMB-FBH crystals.

of the output files were prepared by using Gauss View 5.0. program [30]. The vibrational assignments were done based on potential energy distribution (PED) using VEDA4 program [31]. The molecular surface and fingerprint plots of DMB-FBH were generated with Crystal Explorer 17 software [32] using .cif as the input. The topological properties were carried out using Bader's Quantum Theory of Atoms in Molecules (QTAIM) for the covalent and the strong/weak H-bond interactions in order to reveal the characteristics of open and closed-shell interactions. All these calculations have been performed from AIMALL package [33]. In this approach, the single point calculations were carried out using B3LYP method with 6–311 G (d,p) basis set over the symmetric unit of DMB-FBH in Gaussian 09 software.

2.4. Molecular docking

The crystal structure of *M. tuberculosis* was extracted from the Protein Data Bank (PDB ID: 2 × 22) for the target using protein preparation wizard module. Initially, the protein was minimized with the *OPLS4* force field [34]. The ligand, DMB-FBH, which inhibits the target was neutralized and prepared for induced fit docking (IFD) [35] using the *Epik* program on the *LigPrep* module. Both the modules are inbuilt in the *Schrödinger Maestro* application package [36,37]. The IFD procedure was performed with extra precision (XP) mode [38] and resulted the different conformations of DMB-FBH ligand in the active site of the target enzyme.

3. Results & discussion

3.1. Crystallographic structure and morphology

The theoretical morphology of DMB-FBH crystal was generated using KrystalShaper program [39] as presented in Fig. 1. The crystal facets such as 420, 2$\bar{4}$0, 0$\bar{1}$3, 10$\bar{3}$, 01$\bar{3}$, 103, 013, 0$\bar{1}$3 reveal the tetragonal system of the DMB-FBH crystals. The asymmetric unit is situated in the *ac* plan and the strong N–H···O bonding is directing along *c* axis (Fig. S1). The growth rate is high along the *c* axis as presented in Fig. 1.

The crystal system is tetragonal with centro symmetric space group I 41/a. The cell parameters are $a = 20.7882(7)$ Å, $b = 20.7882(7)$ Å, $c = 14.9162(6)$ Å, $\alpha = 90°$, $\beta = 90°$, and $\gamma = 90°$ with $V = 6446.0(4)$ Å^3. The crystallographic details are presented in Table 1. The hydrogen bond interactions of DMB-FBH are listed in Table 2.

The stability of the DMB-FBH crystal was established by understanding the intermolecular and intramolecular interactions, especially, the H-bonded interactions. The N(2) – H(2) ··· O(1) intermolecular interaction connects the other two molecules on both sides of the asymmetric unit via N(2) – H(2) ··· O(1) as shown in Fig 2. The nitrogen atom in the hydrazide links with O of another hydrazide via hydrogen bonding. Similarly, oxygen atom in the hydrazide links other molecules of N. The connected molecules are antiparallel and perpendicular to the asymmetric unit. The intramolecular interaction exists between the methoxy oxygen and the carbon atom connected to the fluorobenzohydrazide. The ORTEP plot of DMB-FBH is presented in Fig. 3.

All the possible hydrogen bonding interactions are listed in Table S1. (see supplementary information) and they were calculated from PARST module of WINGX package [40]. It is observed that the thermodynamic stability of DMB-FBH crystals was rely on the two weak C–H ···O/N and another two strong N–H···O/N interactions. Despite these interactions, there were H···π and very-weak interactions observed in the crystal packing of DMB-FBH.

3.1.1. Interaction energies

The asymmetric molecules in the crystal phase of DMB-FBH were stabilized by anti-stacking model as shown in Fig 2. As mentioned above, the packing is highly stabilized by N2-H2···O1 interactions. The energies of these interactions are calculated from

Table 1
The crystallographic and refinement details of DMB-FBH crystal.

Chemical formula	$C_{16}H_{15}FN_2O_3$
Cambridge crystallographic data center (CCDC No)	2113509
Formula weight	302.31
Temperature/K	273
Crystal system	tetragonal
Space group	I41/a
a/Å	20.7882(7)
b/Å	20.7882(7)
c/Å	14.9162(6)
α/°	90
β/°	90
γ/°	90
Volume/Å^3	6446.0(4)
Z	16
ρ_{calc}g/cm^3	1.2459
μ/mm^{-1}	0.095
F(000)	2529.5
Crystal size/mm^3	0.07 × 0.07 × 0.07
Radiation	Mo Kα (λ = 0.71073)
2Θ range for data collection/°	5.16 to 54.28
Index ranges	$-26 \le h \le 26$, $-26 \le k \le 26$, $-19 \le l \le 19$
Reflections collected	73176
Independent reflections	3573 [R_{int} = 0.0704, R_{sigma} = 0.0321]
Data/restraints/parameters	3573/0/201
Goodness-of-fit on F^2	1.056
Final R indexes [$I>=2\sigma$ (I)]	R_1 = 0.0553, wR_2 = 0.1340
Final R indexes [all data]	R_1 = 0.0917, wR_2 = 0.1586
Largest diff. peak/hole / e Å^{-3}	0.28/−0.35

Table 2
Hydrogen bond interaction of DMB-FBH crystals.

D – H···A	d(D–H)/Å	d(H···A)/Å	d(D···A)/Å	<(DHA)/°
N(2) – H(2) ··· O(1)#1	0.86	2.25	2.9282 (1)	136
C(8) – H(8) ··· O(2)	0.93	2.42	2.7546	101
C(8) – H(8) ··· N(1) #1	0.93	2.54	3.4063	156
C(12) – H(12) ··· O(1)#2	0.93	2.55	3.3832	149
C(16) – H(16B) ··· O3	0.96	2.55	3.0685	114

Equivalent positions: #1: ¼+*y*, ¼-x, ¼+*z*, #2: -¼+*y*, ¼-x, ¼+*z*.

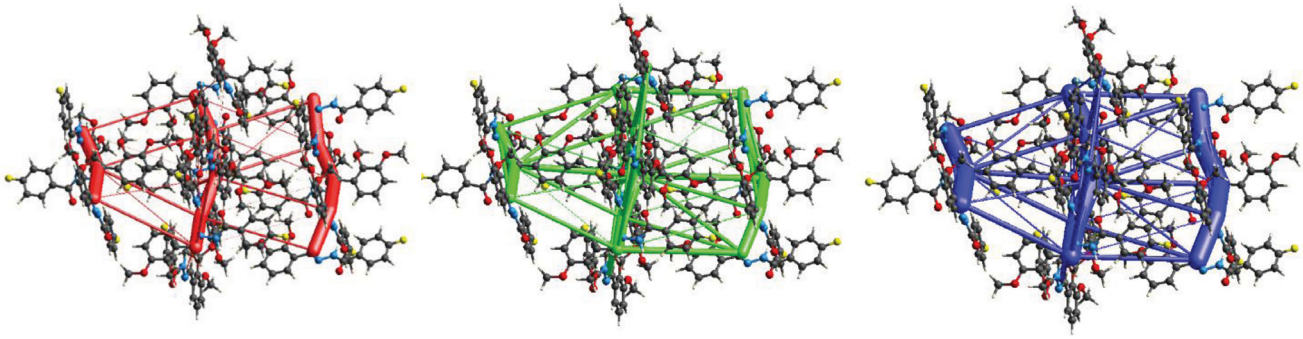

Fig. 4. Energy frameworks (left), coloumb dispersion (center) and total energy (right) of DMB-FBH crystal structure. The crystal is viewed down along the *a* axis. (A cylinder scale of 80 was used for all three energies).

Crystal Explorer 17 package and pixel method [41]. The components of total energy (E_{tot}) are electrostatic, polarization, dispersion and exchange-repulsion, calculated using B3LYP/6–31G** level of theory and finally scaled based on benchmarked energy models. From these calculations, it is predicted that dispersion energy is influenced strongly towards the packing stability and the three-energy frameworks are shown in Fig. 4. The energy values are listed in Table 3. As expected, the N–H···O/N and C–H···O/N interactions are considered as strongest and the corresponding energy values are −75/−67.3 kJ/mol (N2-H2···N1, N2-H2···O1, C8-H8···N1, C5-H5···O1 and C5-H5···N1) and −21.2/−19.3 kJ/mol (C12-H12···O1 and C14-H14···O1) from both Pixel and Crystal Explorer calculations.

Furthermore, the significance of these interactions are emphasized in QTAIM analysis by locating the bond critical point (bcp) in the bond path of the respective H-bond interactions. The topological properties of the closed-shell interactions are given in Table 4, which supports the results obtained from Pixel and Crystal Explorer calculations.

3.1.2. Electrostatic potential in packing

The electrostatic potential plot is shown in Fig. 5 which evidences the existence of the strong potential (red region) in the H-bond interactions [42]. The experimental crystal structure shows a correlation C_{vv} of 67% between the interior and exterior potential (Fig. 6). The regions of highest inner potential correspond to the

Table 3
PIXEL/Crystal Explorer lattice energies (kJ/mol) of DMB-FBH molecular pairs.

S.No	Symm.code	Centroid distance	E_{coul}	E_{pol}	E_{Disp}	E_{Rep}	E_{total}	Main interactions
1	$y + 1/4,-x + 1/4 + 1,+z + 1/4$	3.856	−43.2/ −46.8	−17.4/ −14.9	−49.5/ −48	35.1/ 56.7	−75/ −67.3	C8-H8···N1, N2-H2···N1, C5-H5···O1, C5-H5···N1, N2-H2···O1
2	$y + 3/4,-x + 1/4 + 1,-z + 1/4$	10.118	−9/−10.3	−4.1/ −4.1	−15.7/ −16.5	7.6/ 14.5	−21.2/ −19.3	C12-H12···O1, C14-H14C···O1
3	$-y + 3/4 + 1,+x-1/4,-z + 3/4$	11.36	−0.2/−7.8	−3/−1.9	−4.1/−15.6	10/11.8	−17.3/−15.9	C14-H14B···O2, C14-H14C···O2
4	$X+½,-y, z+½$	10.39	0.2	−1.2	−20.8	5.4	−16.5	O2···O1, C16···H2A, H16A···C2, H16A···H2A, H16B···C3/C2/H2A,H3,
5	$-x + 1/2 + 1,-y + 1,+z + 1/2$	7.586	0.3/−0.6	−2.3/−2.1	−3.6/−15.9	4/6.5	−11.6/12	C16-H16···O1
6	$y + 1/4,-x + 3/4,-z + 3/4$	10.885	−3.4/−3.4	−0.5/−0.4	−5/−6.3	1.1/2	−7.8/−8.1	C6-H6···F1
Pixel Energy	–	–	−67.9	−33.2	−135.7	66.3	−170.5	

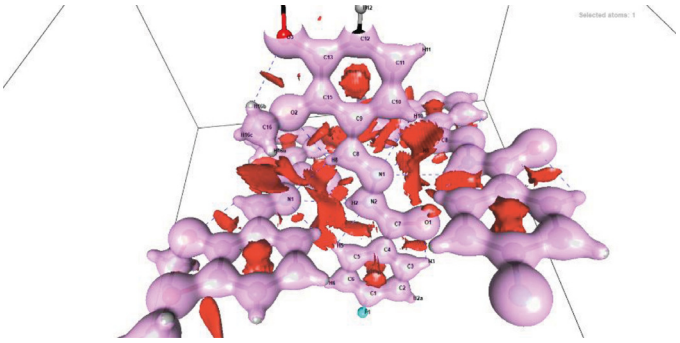

Fig. 5. Electrostatic potential (red region) in the H-bond interactions of DMB-FBH.

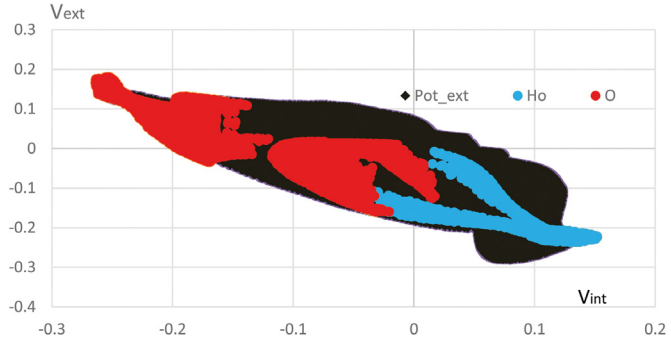

Fig. 6. Scatterplot of inner and outer electrostatic potential *V* on the Hirshfeld surface for the DMB-FBH crystal structure. The contacts donated by oxygen and by the polar hydrogen atom Ho/n from the inner molecule are highlighted in red and blue color, respectively.

polar hydrogen atoms Ho and Hn while oxygen atoms are at the origin of the most electronegative areas. A high anti-correlation is related to a good complementarity of inner and outer potentials.

3.1.3. Hirshfeld surface and quantitative molecular interaction of DMB-FBH compound

The role of intermolecular interactions towards the crystal stability is explored from the Hirshfeld fingerprint analysis calculated from Crystal Explorer 17 package. The Hirshfeld surface quantitatively addresses the information about the molecular surface and interactions. The Hirshfeld denoted surface is an isosurface surrounded by promolecules that represents the volume of the electron density. The nearest nucleaus inside the isosurface (di) and outside the isosurface (de) can generate a 2D plot as a function of distance. Each point in the 3D surface is defined by colors ranging from blue to red in which the former represents the longest distance whereas the latter indicates the closest contact of the molecules. The white color indicates that the d_{norm} is equal to Van der Waals separation (vdW). The red spot in the d_{norm} indicates about the N(2) – H(2) ⋯ O(1) intermolecular hydrogen bonding in the hydrazide of two neighboring molecules. The Hirshfeld surface of DMB-FBH is presented in Fig. S2 (see supplementary information).

In the fingerprint plot of Fig. 7, the two spikes at d_i =1.3, and d_e=1.3 indicate the overall contribution of O⋯H (17.6%) which makes the strong impact over the stability of the DMB-FBH crystal. The other different interactions between the elements presented in DMB-FBH are listed in Table S4 (see supplementary information). The center tip at 1.2 Å is H–H interaction with 39.3% and the adjacent tip is associated with O–H interaction (8.8%). The latter interaction is also overlapped with N–H interaction (4%). The π-π interaction (C–C) in DMB-FBH is 4% around 2.0 Å. The fluorine hydrogen interaction is significantly high about 5.2% and their parallel

Table 4
Topological properties at the critical points of intermolecular interactions. The *G*, *V* and *H* are the kinetic, potential and total energy density respectively. The $E_{Hbond} = ½\ V(\mathbf{r})$ bond is the dissociation energy as described in [42].

Interaction	Density ρ (e/Å^3)	Laplacian (e/Å^5)	$G(\mathbf{r})$ (a.u.)	$V(\mathbf{r})$ (a.u.)	$H(\mathbf{r})$ (kJ/B^3/mol)	E_{Hbond} (kJ/mol)
C8-H8...N1*	0.062	0.709	0.043	−0.037	0.006	−0.019
N2-H2...N1*	0.050	0.685	0.040	−0.032	0.008	−0.016
C5-H5...N1*	0.029	0.328	0.018	−0.014	0.005	−0.007
N2-H2...O1*	0.098	1.267	0.083	−0.078	0.006	−0.039
O1...TYR158	0.142	1.460	0.015	−0.017	0.002	−0.008
O3...LYS165	0.111	1.100	0.013	−0.012	0.001	−0.006

* $y + 1/4,-x + 1/4 + 1,+z + 1/4$.

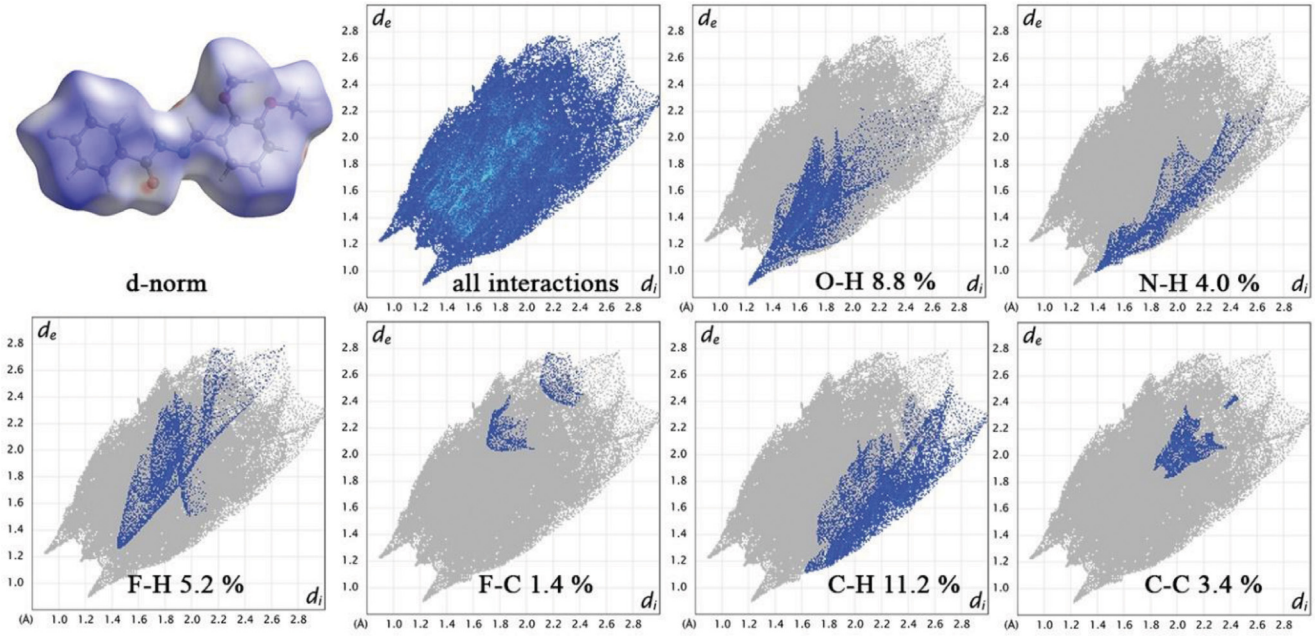

Fig. 7. Hirshfeld surface and fingerprint plot of DMB-FBH compound.

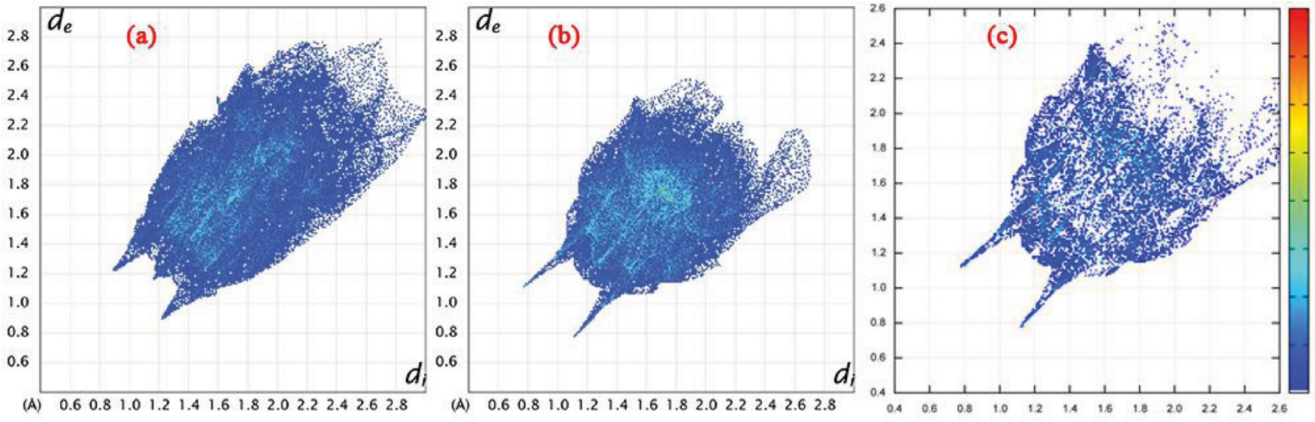

Fig. 8. The 2-dimensional Hirshfeld finger print plot of DMB-FBH (a), similar structure, (E)-N′-(3,4-dimethoxybenzylidene)furan-2-carbohydrazide (b) and traces left behind in the difference plot over DMB-FBH (c).

effect in fluorescence emission has been discussed in Section 3.6. The aromatic ring interactions and their interaction with fluorine are 11.2 and 1.4% respectively.

Furthermore, the fingerprint plot of DMB-FBH (Fig. 8(a)) was compared with previously reported similar molecule, named (E)-N′-(3,4-dimethoxybenzylidene)furan-2-carbohydrazide. In this structure, when comparing with DMB-FBH the fluorrobenzo hydrazide is replaced by the five ring furan. The five ring furan crystal (Fig. 8(b)) has strong contributions over DMB-FBH interactions towards the crystal stability. For instance, the O···H, N···H, C···C and C···H internactions are respectively 12.6%, 3.8%, 2.3% and 14.1% for O···H, N···H, C···C and C···H which was well explored from the traces left behind in the difference plot as portraited in the Fig. 8(c).

3.2. Optimised molecular geometry

The optimized structures of DMB-FBH are presented in Fig. 9. The DMB-FBH compound consists of 37 atoms and thus the 105 vi-

Table 5
Selected geometric parameters of DMB-FBH obtained by B3LYP/6–311 G (d,p).

Bond Length (Å)	B3LYP/ 6–311G(d,p)	Single crystal XRD	Bond Angle (Å)	B3LYP/ 6–311G(d,p)	Single crystal XRD
O1-C9	1.37	1.373	C9-O1-C15	116.34	114.53
O1-C15	1.4343	1.415	N4-N3-C6	120.92	118.71
O2-C6	1.21	1.22	N3-N4-C7	116.96	114.75
N3-N4	1.3564	1.381	C12-O5-C21	118.33	116.67
N3-C6	1.3877	1.346	O2-C6-N3	123.39	121.9
N4-C7	1.2808	1.271	O2-C6-C10	122.36	121.31
O5-C12	1.365	1.36	N3-C6-C10	114.23	116.79
O5-C21	1.4213	1.428	N4-C7-C8	121.11	121.72
C6-C10	1.5032	1.488	C7-C8-C9	119.19	118.1
C7-C8	1.4635	1.459	C6-C10-C13	116.94	117.64
C8-C9	1.4023	1.387	O5-C12-C9	115.73	115.12
C8-C14	1.4071	1.393	F11-C20-C18	118.99	118.4
C9-C12	1.412	1.402			
C10-C13	1.3999	1.385			
C10-C16	1.4001	1.346			
F11-C20	1.3489	1.353			
C12-C17	1.3925	1.374			
C13-C18	1.3883	1.382			
C14-C19	1.3809	1.367			
C16-C22	1.3918	1.383			
C17-C19	1.3996	1.381			
C18-C20	1.3882	1.351			
C20-C22	1.3865	1.349			

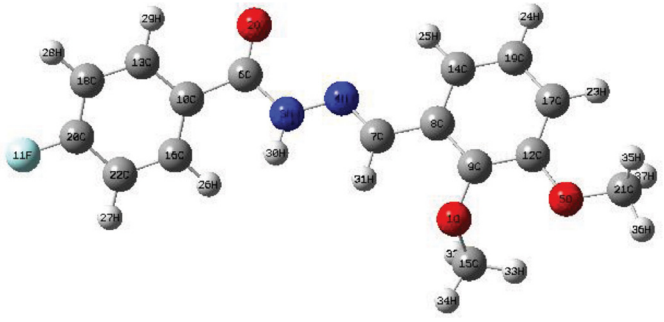

Fig. 9. Optimized molecular structure of DMB-FBH compound at gas phase.

brational modes are observed. The selected bond lengths and bond angles are listed in Table 5. The observed bond length values for O1-C9, N3-N4 and C7-C8 are found to be 1.37, 1.35 and 1.46 Å respectively. The observed bond length between C6–O2 in the carbonyl (C = O) double bond is 1.22 Å and its corresponding theoretical value is 1.21 Å . The C = O molecular interaction with the π free electronic pairs of N3 and N4 nitrogen atoms are part of electronic pairs of O atom which compensates the electronic effect issued from this conjugation, therefore C6–O2 bond length does not vary significantly. All the geometric parameters of DMB-FBH compound obtained by B3LYP/6–311 G (d,p) are in good agreement with the single crystal data.

3.2.1. ^{1}H &^{13}C NMR spectral study

The theoretical ^{1}H NMR and ^{13}C NMR spectra of the DMB-FBH compound is shown in Fig. 10 and their shift are listed in Table S2. The chemical shift value of azomethine proton is assigned at 8.07 ppm. Two sets of computed chemical shifts observed from 8.29 to 7.42 and 7.16–6.98 ppm are due to four aromatic protons of meta and ortho positions of fluorine substituted in the phenyl ring. The six hydrogen atoms associated to two methoxy group are observed in the region δ= 3.07–4.62 ppm. This downfield shifts of oxygen atom attached to methyl groups is resulted in the reduction of electron densities around the methyl groups [43]. The downfield chemical shift were respectively observed at 161.00, 153.40, 159.00 and 172.72 ppm for C6, C9, C12 and C20. It is due to the descreening effect of electronegative fluorine and oxygen atom. The upfield peaks at 58.63 and 53.91 ppm are attributed to the methyl groups of two methoxy carbons. For phenyl rings, the shift related to aromatic carbons are greater than 100 ppm for DMB-FBH.

3.2.2. Vibrational spectral analysis

The theoretical and experimental FTIR spectra of DMB-FBH are presented in Fig. 11. The detailed vibrational wavenumbers are assigned by potential energy distributions (PED) analysis. Both experimental and theoretical wavenumbers with the PED contributions of DMB-FBH are presented in Supplementary Table S3 (see supplementary information). The C–H vibrations of heteroaromatic organic compounds has consisted of multiple weak bands in the region 3100–3000 cm^{-1} [25]. In present study, the aromatic ring C–H stretching frequencies such as $\nu C_{13}H_{29}$, $\nu C_{14}H_{25}$, $\nu C_{18}H_{28}$, $\nu C_{17}H_{23}$, $\nu C_{22}H_{27}$, $\nu C_{16}H_{26}$ and $\nu C_{19}H_{24}$ occur around the region 3055–3054 cm^{-1} and 3087–3081 cm^{-1}. The medium peak observed at 2913 and 2842 cm^{-1} are related to C–H stretching band of dimethoxy substituted aromatic ring. The νN–H modes are expected to occur in the region 3200–3400 cm^{-1} [44]. The theoretical νN_3H_{30} peak is observed at 3368 cm^{-1} with 100% PED, while the experimental FT-IR peak is traced at 3432 cm^{-1}. The theoretical vibrational peak of C–N stretching skeletal bands are projected to occur at 1450 cm^{-1} which also overlap with other vibrational modes [45]. The theoretical νN_4C_7 stretching peak is observed at 1608 cm^{-1} and νN_3C_6 is at 1495 cm^{-1}. The corresponding experimental FT-IR peaks are observed at 1414 cm^{-1}. The C = O stretching mode is expected in the spectral range of 1750–1650 cm^{-1} [46]. The theoretical νO_2C_6 is at 1705 cm^{-1}, but the experimental FT-IR band is observed at 1600 cm^{-1} with 85% of PED. The νN4N3 is the bridge between aldehyde and hydrazide which occurs at 1117 cm^{-1} in the experimental FT-IR and 1126 cm^{-1} in the DFT. The ν $F_{11}C_{20}$ is observed at 577 cm^{-1}. The calculated frequencies are usually higher than the corresponding experimental quantities, due to the combination of electron correlation effects and basis set deficiencies.

3.3. Highest occupied molecular orbital and lowest unoccupied molecular orbital (HOMO-LUMO) analysis of dmb-fbh compound

The HOMO-LUMO energies of the compound provide information about energetic behavior and stability [47]. The HOMO-LUMO

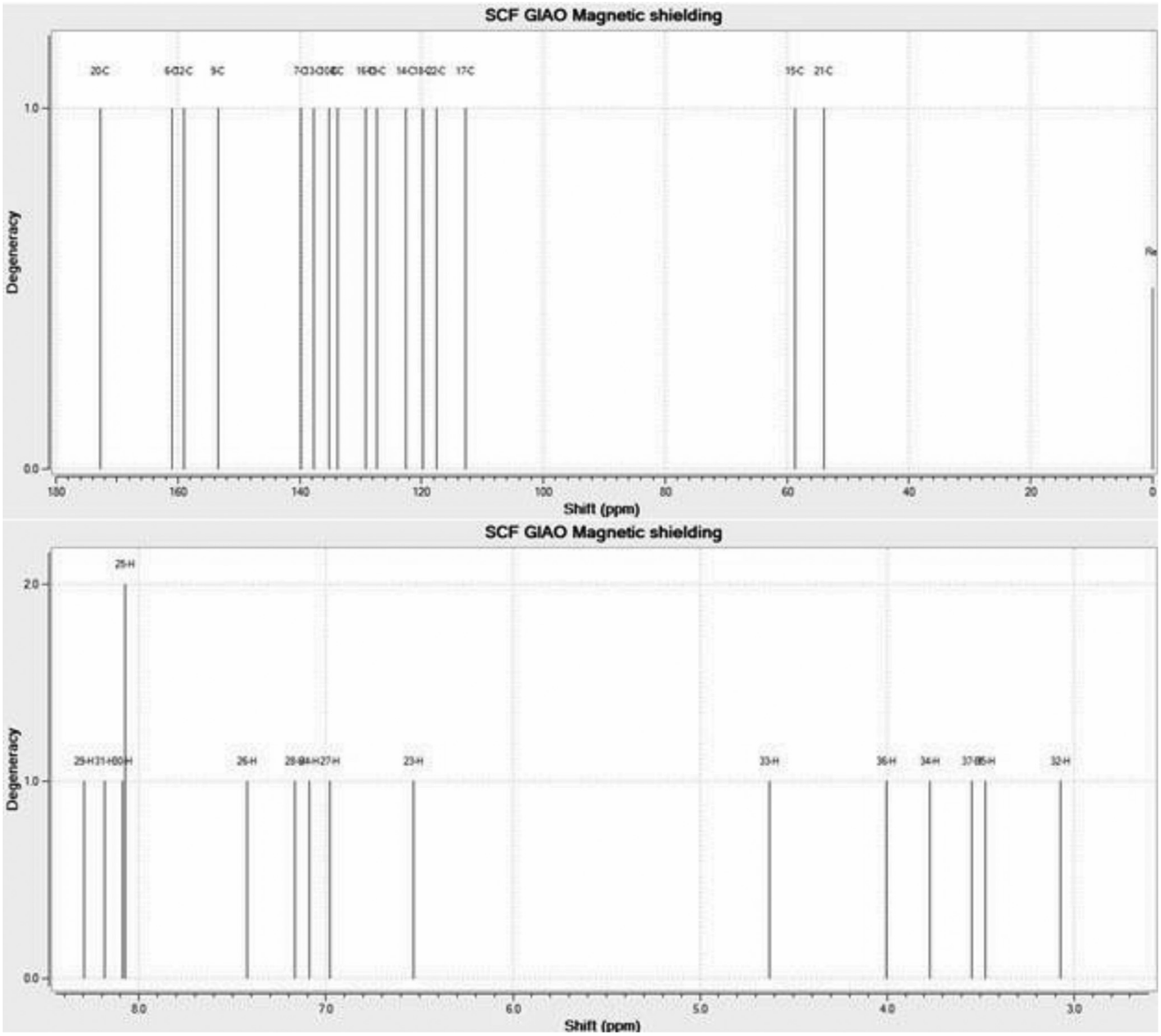

Fig. 10. Theoretical ^{1}H NMR (top) and ^{13}C NMR (bottom) spectra of the DMB-FBH compound.

Table 6
The calculated parameters of frontier molecular orbitals.

Parameters (ev)	B3LYP/ 6–311 G (d,p)
E_{HOMO}	−6.0997
E_{LUMO}	−1.7115
Ionization potential (I)	6.0997
Electron affinity (A)	1.7115
Energy gap = ΔE	4.3881
Electronegativity (χ)	3.9056
Chemical potential (μ)	−3.9056
Chemical hardness (η)	4.3882
Chemical softness (S)	0.1139
electrophilicity index (ω)	1.738

energy calculations were performed by time-dependent density functional theory (TD-DFT) approach at the B3LYP/6–311 G level. The calculated parameters related to frontier molecular orbitals are presented in Table 6. The HOMO and LUMO pictogram represents the high- and low-density regions as shown in Fig. 12. The HOMO is mainly delocalized at the 2,3-dimethoxy benzaldehyde and hydrazide regions which connects the 4-fluorobenzohydrazide moieties, whereas the LUMO is delocalized and spread over the entire molecular structures. The charge delocalizations were further shifted to both ends of the DMB-FBH for HUMO-1 and LUMO+1 which clearly indicates the tendency of complete charge transfer between two moieties at the higher energy levels. The benzohydrazide ring is more planar concerning hydrazide nitrogen whereas dimethoxy benzaldehyde is out of plan. As a result, the conjugation is increasing for intramolecular charge transfer (ICT) [48]. This kind of ICT plays fundamental role in deciding properties of molecular crystals for non-linear optical applications (push-pull charge transfer interaction) [38], organic light-emitting diode [39] and sensors to mention a few. The calculated energy values of HOMO, LUMO and HUMO-1, LUMO+1 are −6.099706 eV, −1.711596 eV and −6.20855 eV, −0.97444 eV, respectively. The energy gap value between the HOMO and LUMO is 4.38811 eV, and HOMO-1 and LUMO+1 is 5.23411 eV. Instead of 2,3-dimethoxybenzaldehyde, the compound synthesized with the precursor of 4-chlorbenzaldehyde shows similar HOMO-LUMO energy gap (4.2958 eV) [45] indicating that the methoxy or chloro substituted in the molecular moieties

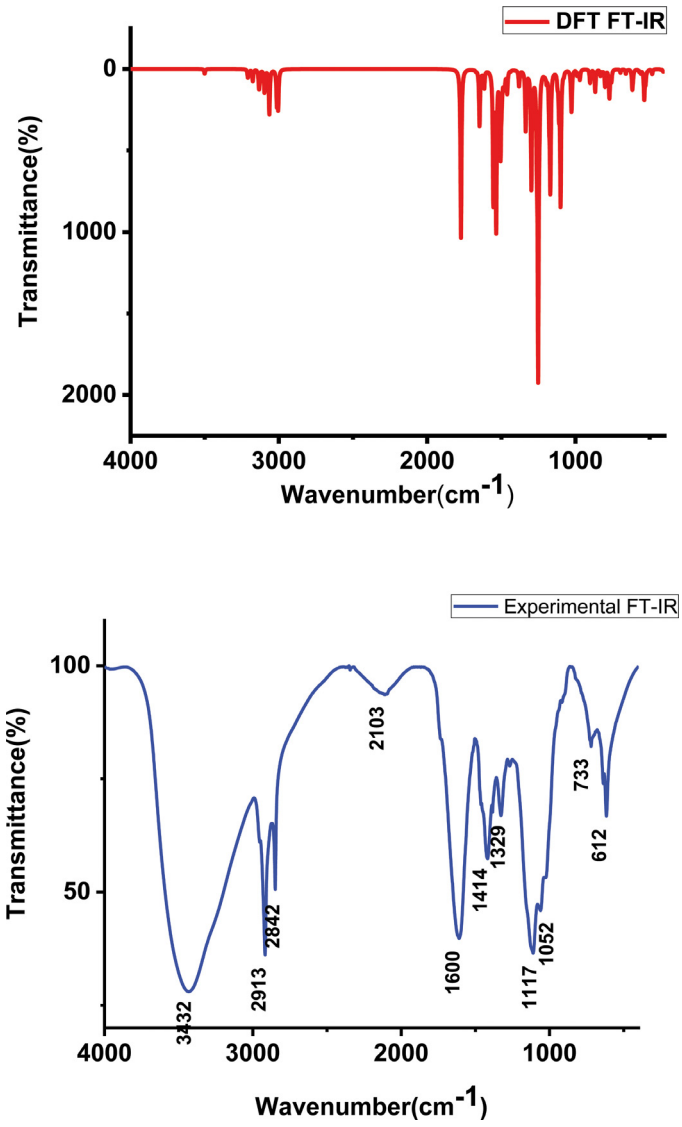

Fig. 11. The theoretical (top) and experimental FT-IR spectra of DMB-FBH compound.

does not significantly effect the charge transfer process resulted in similar conjugation length.

3.4. Nonlinear optical properties and dipole moment of dmb-fbh compound

The theoretically calculated polarizability (α), the anisotropy of polarizability ($\Delta\alpha$), first order molecular hyperpolarizability (β), and dipole moment (μ) of DMB-FBH are presented in Table 7. The total dipole moment (μ) and the first order hyperpolarizability (β) of DMB-FBH were calculated as 5.2478 and 3.821 $\times$ 10^{-30} esu respectively. The value of β was 10 times higher than the standard urea (0.1947 $\times$ 10^{-30} esu). Though it is inappropriate to consider the hyperpolarizability β for the centrosymmetric space group ($I4_1/a$) of DMB-FBH molecule, the remarkable increase of molecular hyperpolarizability indicates the feasibility of large migration of charges from donor to acceptor moieties [49].

3.5. Thermogravimetric/Differential thermal analysis

The thermogravimetric and differential scanning calorimetry (TG/DSC) of DMB-FBH is presented in Fig. 13. The endothermic peak of DMB-FBH is observed at 162 °C which is significantly high among the other organic systems for e.g. sugar alcohols such as glucose and fructose [50]. This value is equal [46] or less than the organic salt [44]. It indicates that the DMB-FBH possesses strong inter and intramolecular interactions in the crystal structure. This result further confirms the strong hydrogen bond interaction as discussed in the Section 3.1 and Section 3.5. The enthalpy of DMB-FBH is 68.81 J/g obtained from first derivatives of DSC. This enthalpy is low as the decomposition starts after the melting point. There is no exothermic or endothermic peak that occurs before the melting peak indicating that the DMB-FBH is moisture free and stable upto 162 °C. In DMB-FBH, the first stage of decomposition occurs with 89% weight loss and rest of the weight loss occurs until 600 °C. The 2,3-dimethoxybenzaldehyde along with few moieties in hydrazide has probably removed at first from the DMB-FBH because the thermogram shows high weight loss and their stability is low compared with 4-fluorobenzohydrazide.

Table 7
Nonlinear optical parameters of DMB-FBH compound.

Parameters	B3LYP/ 6–311 G (d,p)	Parameters	B3LYP/6–311 G (d,p)
μ_x	3.7623	β_{xxx}	14.71
μ_y	3.6438	β_{xxy}	−50.36
μ_z	0.3284	β_{xyy}	23.41
μ(D)	5.2478	β_{yyy}	−6.61
α_{xx}	333.9411	β_{zxx}	−326.71
α_{xy}	92.038039	β_{xyz}	−154.57
α_{yy}	135.47052	β_{zyy}	−36.64
α_{xz}	23.046586	β_{xzz}	−176.51
α_{yz}	10.654093	β_{yzz}	−124.76
α_{zz}	213.92388	β_{zzz}	−15.43
α_0(e.s.u)	3.8713 $\times$ 10^{-23}	β_{tot} (e.s.u)	3.821 $\times$ 10^{-30}
α(e.s.u)	3.3768 $\times$ 10^{-23}		

3.6. UV–Vis-NIR transmittance and fluorescence emission studies

The UV–Vis NIR spectrum of DMB-FBH recorded in the aqueous solution is presented in Fig. 14. The absorption peak is observed at 277 nm. The aromatic benzylidene and hydrazide are the chromophores responsible for electronic transition involved in the DMB-FBH. This absorption peak is due to π -π^* transition and intramolecular charge transfer process [51]. There is no significant absorption observed in the visible region of the DMB-FBH. The bandgap energy from absorption value is calculated to be 4.475 eV. This energy gap is indicating the dielectric nature of the crystals therefore with the advantages of transmittances, this crystal can be considered for optical and photonic applications.

The fluorescence emission spectrum of DMB-FBH is presented in Fig. 15. Though the emission intensity is not strong, the blue emission at 450 nm was traced for the excitation of 277 nm. The fluorescence emission from organic materials is associated to the π-conjugation and to the donor-acceptor (D-A) framework featuring electron delocalization [52]. The out-of-planar molecular geometry and both strong intra and intermolecular interaction are considered to be important for the fluorescence emission of DMB-FBH. The fluorine presented in the DMB-FBH does not contribute to fluorescence emission. The fluorescence emission was also recorded for ethanol solution but it shows very weak emission (not reported).

3.7. Third order nonlinear optical studies

The normalized closed aperture (CA) Z-scan curves obtained from DMB-FBH in ethanol solution is shown in Fig. 16(a). The calculated Rayleigh range is 3.1 mm and the calculated values of β, n_2 and $\chi^{(3)}$ are listed in Table 8.

Table 8
Third-order nonlinear optical parameters of DMB-FBH in ethanol solution.

n_o	n_2 (cm^2/W)	β (cm/W)	$Re\chi^{(3)}$ (cm^2/W)	$Im\chi^{(3)}$ (cm/W)	$\chi^{(3)}$ (esu)
2.454078	5.04×10^{-9}	3.70×10^{-4}	4.64×10^{-6}	2.82×10^{-7}	4.65×10^{-6}

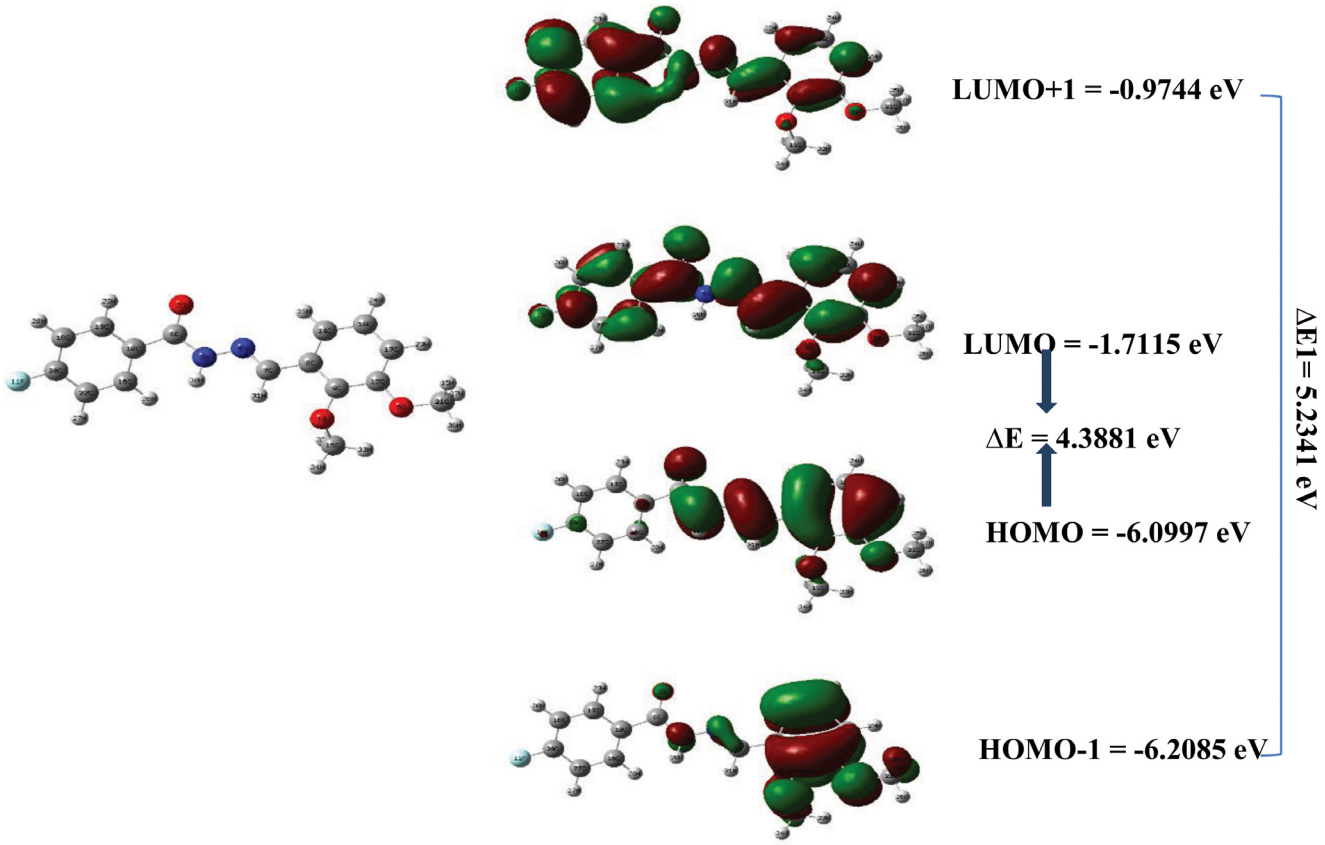

Fig. 12. The optimized molecular structure (left) and different HOMO, LUMO levels (right) of DMB-FBH compound.

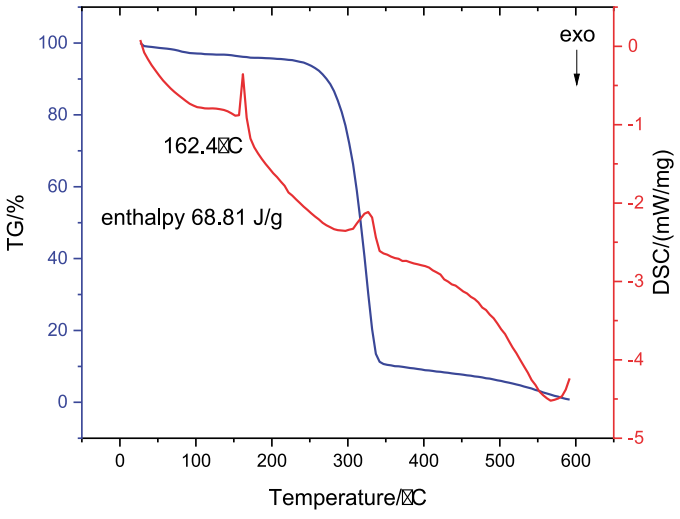

Fig. 13. Thermogravimetric and differential thermal analysis of DMB-FBH crystals.

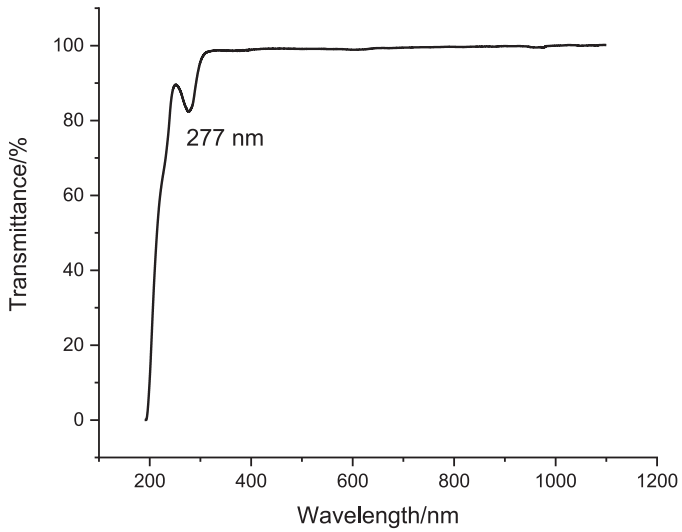

Fig. 14. The transmittance spectrum of DMB-FBH crystals in aqueous solution.

The normalized closed aperture (CA) Z-scan curves obtained from ethanol solutions of DMB-FBH is presented in Fig. 15(a). The CA curves for DMB-FBH exhibited a pre-focal peak centered at −0.96 mm followed by a post-focal valley configuration pointed at 0.92 mm. This peakvalley configuration indicates that the nonlinear refractive index is negative ($n2 < 0$) which gives rise to the self-defocusing property. The self-defocusing effect is due to local variation of refractive index with temperature.

Table 9
Comparison of first order hyperpolarizability of the derivatives of benzohydrazide.

Compound name	Nonlinear absorption coefficient (β)	References
(*E*)-*N*′-(benzo[*d*][1,3]dioxol-5-ylmethylene)−4-methoxybezohydrazide monohydrate	2.39 × 10^{-5} cm/W	39
{(1Z)-[4-(D*imethylamino*)*phenyl*]methylene} 4-nitrobenzocarboxy hydrazone mono-hydrate	8.62 × 10^{-7} cm/W	40
2-(4-chlorophenoxy)-N′-[(1E)−1-(4-*methylphenyl*) *ethylidene*]acetohydrazide	2.48 × 10^{-6} cm/W	41
(E)-N′-(2,3-dimethoxybenzylidene)−4-fluorobenzohydrazide	3.70 × 10^{-4} cm/W	Present work

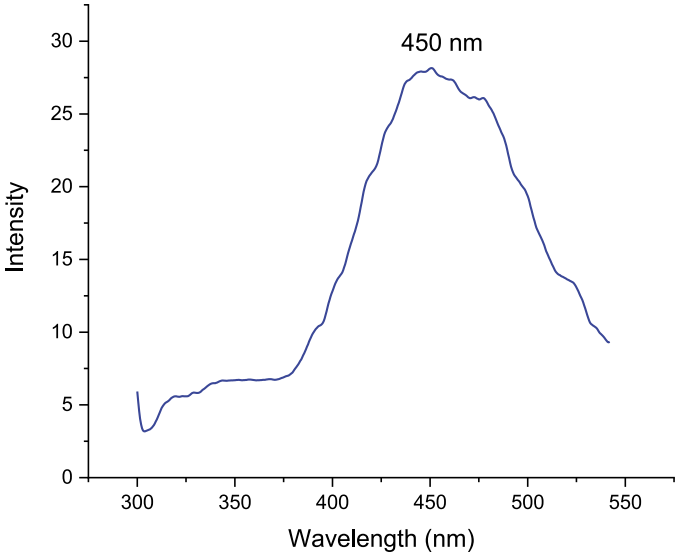

Fig. 15. Fluorescence emission spectrum of DMB-FBH in aqueous solution. The peak at 450 nm is related to blue region.

The third-order nonlinear refractive index (n_2) of the DMB-FBH was calculated using closed aperture data, and it is given by

$$n_2 = \frac{\Delta\Phi}{KI_0L_{eff}} \tag{1}$$

where K represents the wave vector [$K = \frac{2\pi}{\lambda}$], L_{eff} represents the sample's effective thickness, and α is the linear absorption.

The experimentally obtained open aperture curve of DMB-FBH is shown in Fig. 15(b) which has reverse saturable absorption behavior. The material with reverse saturable absorption (RSA) behavior shows ultra-fast response time as compared to saturable absorption (SA). The equation for nonlinear transmittance for open aperture Z scan data, fitted with two-photon absorption (TPA) model, is given by

$$T(Z) = \left[1 - \frac{\beta\ I_0\ L_{eff}}{2\sqrt{2}\left(1 - \frac{Z^2}{Z_0^2}\right)}\right] \tag{2}$$

where, T (z) is the normalized transmittance, I_0 is the intensity at the focus, and L_{eff} is the effective length of the sample. From the open aperture, the nonlinear absorption coefficient (β) is as given below

$$\beta = \frac{2\sqrt{2}\ .\Delta T}{I_0L_{eff}} \tag{3}$$

where ΔT is the highest value in plot. The experimentally observed β value is 3.70 × 10^{-4} cm/W.

The real and imaginary parts of the third-order susceptibility relation are given in equs 4 and 5 respectively,

$$R_e\chi^{(3)} = \frac{10^{-4}\varepsilon_0C^2n_2n_0^2}{\pi} \tag{4}$$

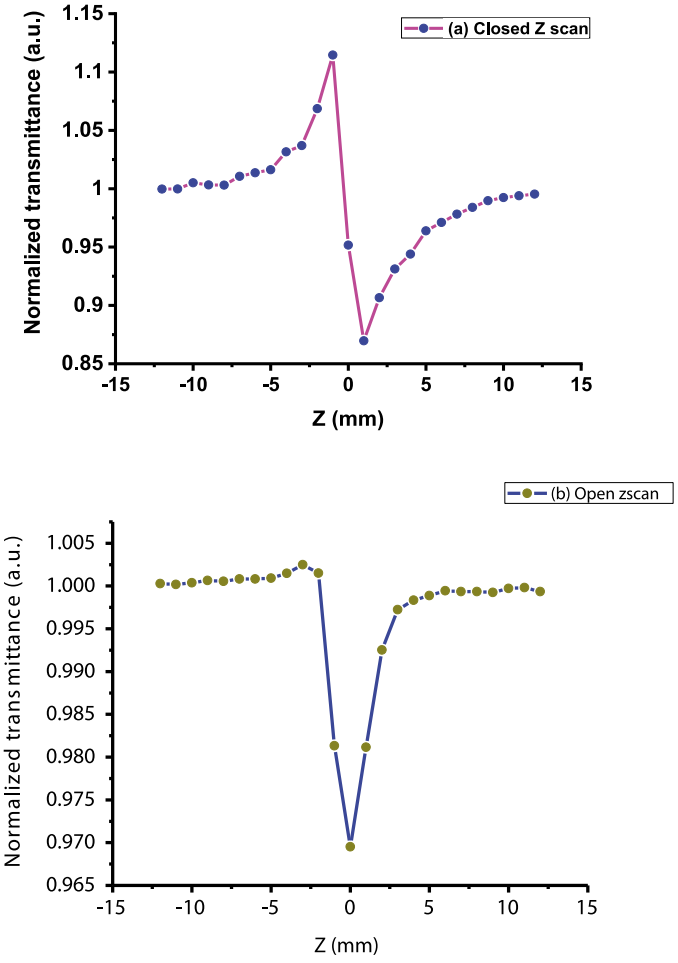

Fig. 16. Closed (a) and open (b) Z-scan curves of DMB-FBH in ethanol solution.

$$I_m\chi^{(3)} = \frac{10^{-2}\varepsilon_0C^2n_0^2\ \lambda\beta}{\pi} \tag{5}$$

Here, the permittivity of free space ε_0 = 8.8518 × 10^{-12} Fm^{-1}, the linear refractive index (n_0) and c is the velocity of the light in space. The real and imaginary parts of third-order nonlinear optical susceptibility $\chi^{(3)}$ was calculated by the relation.

$$\chi^{(3)} = \sqrt{\left\{R_e\left(\chi^{(3)}\right)^2 + I_m\left(\chi^{(3)}\right)^2\right\}} \tag{6}$$

The value of nonlinear absorption coefficient of DMB-FBH is β = 3.70 × 10^{-4} cm/W *and* third order susceptibility $\chi^{(3)}$ = 4.65 × 10^{-6} esu. The third-order susceptibility is reasonably larger than the other benzohydrazide derivatives which are compared as listed in Table 9 [53–55].

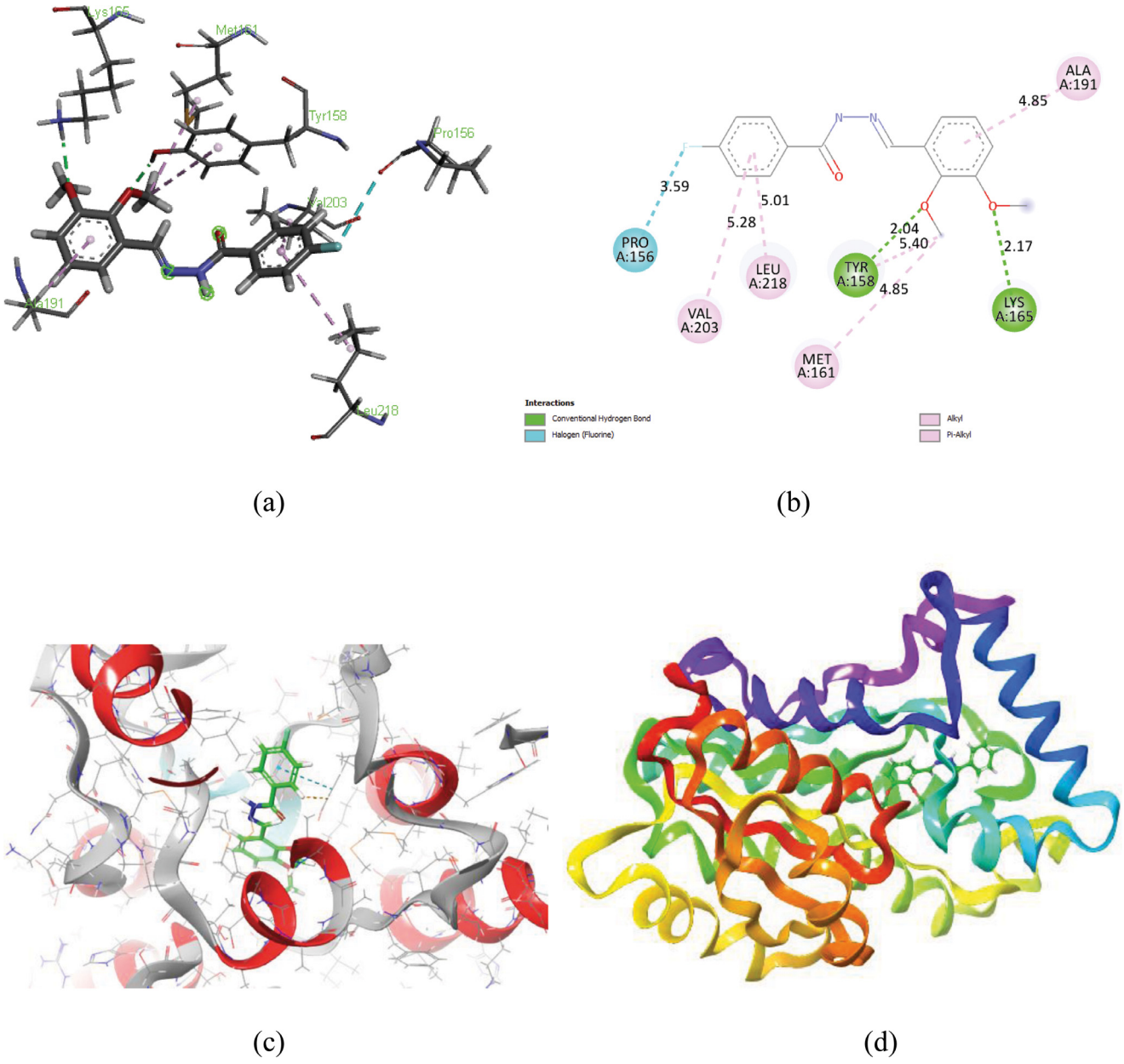

Fig. 17. Intermolecular interactios and the orientation of DMB-FBH in the active site of *M. tuberculosis*.

3.8. *DMB-FBH* - M. tuberculosis *binding*

To understand the intermolecular interaction of DMB-FBH in the active site of *M. tuberculosis* enzyme, the IFD method was carried out. The docking score, glide energy and IFD values of different conformations of ligand-protein complex are listed in Table 10 and their lowest values are −9.132 Kcal/mol, −39.864 Kcal/mol and −534.19 Kcal/mol respectively. It is to be noted that the residues were involved as expected in the interactions with the DMB-FBH ligand. Table 11 provides the significant intermolecular interactions between the ligand atoms and active site amino acids of target protein. The DMB-FBH makes strong hydrogen bond interactions with TYR158, and LYS165, and their interaction distances are 2.038 Å, and 2.168 Å, respectively. In addition, the hydrophobic and halogen interactions were framed with VAL203, LEU218, ALA191 and PRO156 amino acid residues. Fig. 17 shows the interactions of DMB-FBH molecules in the active site of *M. tuberculosis* revealing the orientation of the molecule. The QTAIM analysis was carried out to validate the strength of these interactions. As expected the H-bond interactions previled in the active site has highly influenced towards the stability of ligand in the active site of the protein. From the Table 4, it is to be concluded that the H-bonding

Table 10
The score and energy (kcal/mol) values of different conformers of ligand-protein complex computed from the molecular docking simulations.

Conformer	Docking score	Glide energy	IFD score
1	−9.132	−39.864	−534.19
2	−8.547	−37.654	−533.71
3	−8.808	−41.399	−533.71
4	−8.57	−43.573	−533.67
5	−8.759	−41.611	−533.33
6	−8.578	−39.345	−532.98
7	−8.421	−41.736	−532.95
8	−8.316	−37.997	−532.94
9	−8.183	−38.501	−532.64

Table 11
Important intermolecular interactions and short contact distances (Å) between the ligand atoms and the active site amino acids of *M. tuberculosis* obtained from molecular docking.

Interaction	Distance (Å)	Type
O1...TYR158:HH	2.038	Hydrogen Bond
O3...LYS165:HZ2	2.168	Hydrogen Bond
F1...PRO156:O	3.594	Halogen Bond
Fluorobenzene...VAL203	5.276	Hydrophobic
Fluorobenzene...LEU218	5.015	Hydrophobic
dimethoxybenzene...ALA191	4.848	Hydrophobic

interactions via oxygen atoms of methoxy groups with TYR158, and LYS165 are found to be stronger as their Laplacian of electron density values were 1.46 e/Å^5 , and 1.10 e/Å^5.

4. Conclusions

The new hydrazone derivative of (E)-N′-(2,3-dimethoxybenzylidene)−4-fluorobenzohydrazide (DMB-FBH) was synthesized and crystals were grown by slow evaporation crystallization from ethanol solution. The N–H···O interaction in DMB-FBH has extended along the c axis resulted in high growth in this direction to produce needle crystals. The interaction energy of the DMB-FBH was calculated by Pixel and Crystal Explorer calculations and contribution of N–H···O/N and C–H···O/N interactions played a role towards the packing stability. The topological analysis based on Bader's Quantum Theory further confirmed the results. The theoretical bond length and bond angle were matched with their experimental crystallographic data. The benzohydrazide ring was more planar concerning hydrazide nitrogen whereas dimethoxy benzaldehyde was out of plan. As a result, the conjugation has increased for intramolecular charge transfer (ICT) as depicted by HOMO-LUMO pictogram. The high contribution of OH interaction further confirmed the role of hydrogen bonds in the stability of DMB-FBH. The UV absorption peak was observed at 277 nm indicating the π -π^* transition. From the antimycobacterial study against the M. tuberculosis, the H-bond interactions previled in the active site has highly influenced towards the stability of ligand in the active site of the protein. The blue emission at 450 nm was observed in DMB-FBH. The melting point of DMB-FBH was 162 °C and the sample decomposed at 340 °C. The nonlinear absorption coefficient (β) was 3.70 × 10–4 cm/W which has nearly two times higher than other hydrazones derivates.

Declaration of Competing Interest

The authors declare that they have no known competing financial interests or personal relationships that could have appeared to influence the work reported in this paper.

CRediT authorship contribution statement

Jeeva P: Conceptualization, Methodology, Software, Writing – review & editing. **Barathi D:** Supervision, Software, Validation. **Rajaboopathi Mani:** Investigation, Software, Writing – review & editing. **David Stephen A:** Software, Investigation, Visualization, Writing – review & editing. **Marjatta Louhi-Kultanen:** Writing – review & editing, Validation. **Vinitha G:** Investigation. **Abdullah G. Al-Sehemi:** Software, Investigation.

Acknowledgements

The authors are thankful to Indian Institute of Technology Hyderabad, India, and Periyar University, Salem, India for providing X-ray diffraction and spectral measurements. The authors are also thankful to the Deanship of Scientific Research at King Khalid University for the funding support through the Research Group Project under Grant number R.G.P.2/22/42.

Supplementary materials

Supplementary material associated with this article can be found, in the online version, at doi:10.1016/j.molstruc.2022.132375.

References

[1] R. Sreedharan, S. Ravi, K.R. Raghi, T.K.M. Kumar, K. Naseema, Growth, linear-nonlinear optical studies and quantum chemistry formalism on an organic NLO crystal for opto-electronic applications: experimental and theoretical approach, SN Appl. Sci. 2 (2020) 1–18.
[2] V. Thayanithi, P.P. Kumar, Investigation on optical, laser damage threshold and non linear optical behavior of creatininium p-toluenesulfonate crystal for electro-optical applications, J. Mater. Sci. Mater. Electron. 31 (2020) 22098–22106.
[3] K. Senthil, S. Kalainathan, F. Hamada, M. Yamada, P.G. Aravindan, Synthesis, growth, structural and HOMO and LUMO, MEP analysis of a new stilbazolium derivative crystal: a enhanced third-order NLO properties with a high laser-induced damage threshold for NLO applications, Opt. Mater. (Amst). 46 (2015) 565–577.
[4] K. Rajesh, A. Mani, K. Anandan, P.P. Kumar, Crystal and optical perfection, linear and nonlinear optical qualities of β alanine β alaninium picrate (βAβAP) single crystal: a promising NLO crystal for optics and photonics applications, J. Mater. Sci. Mater. Electron. 28 (2017) 11446–11454.
[5] S. Kandhan, B.T. Arasan, P. Krishnan, S. Aravindhan, S. Srinivasan, S. Gunasekaran, Structural, optical and piezoelectric investigation on brucinium bromide hydrate non linear optical single crystal for optical parametric oscillators, high-power laser, piezo-sensors and transducers applications, J. Mol. Struct. 1180 (2019) 512–522.
[6] C. Amsaraj, R. Bharathikannan, P. Muthuraja, M. Rajkumar, Analyzing integrated π... π, CH... π and hydrogen bonding interactions in N, N-Dimethyl-4-aminopyridinium benzilate, J. Mol. Struct. 1242 (2021) 130717.
[7] M.C. Sreenath, I.H. Joe, V.K. Rastogi, Experimental and theoretical investigation of third-order nonlinear optical properties of azo dye 1-(2, 5-Dimethoxy-phenylazo)-naphthalen-2-ol by Z-scan technique and quantum chemical computations, Dye. Pigment. 157 (2018) 163–178.
[8] C.W. Sinagra III, F.O. Saouma, C.O. Otieno, S.H. Lapidus, J.-.H. Zhang, A.J. Craig, P. Grima-Gallardo, J.A. Brant, K.A. Rosmus, K.E. Rosello, Synthesis, structure, linear and nonlinear optical properties of noncentrosymmetric quaternary diamond-like semiconductors, Cu2ZnGeSe4 (CZGSe) and the novel Cu4ZnGe2Se7, J. Alloys Compd. 888 (2021) 161499.
[9] R. Narang, B. Narasimhan, S. Sharma, A review on biological activities and chemical synthesis of hydrazide derivatives, Curr. Med. Chem. 19 (2012) 569–612.
[10] J.K.R. Deka, B. Sahariah, K. Baruah, A.K. Bar, B.K. Sarma, Conformational control of N-methyl-N, N′-diacylhydrazines by noncovalent carbon bonding in solution, Chem. Commun. 56 (2020) 4874–4877.
[11] A.M. Mkadmh, R.Y. Morjan, J. Raftery, A.M. Awadallah, J.M. Gardiner, Synthesis, structural characterization, and computational study of (E)-N′-(3, 4-dimethoxybenzylidene) furan-2-carbohydrazide, Arab. J. Chem. 13 (2020) 3571–3584.
[12] F. Zhi, N. Shao, Q. Wang, Y. Zhang, R. Wang, Y. Yang, Crystal structures and antibacterial activity of hydrazone derivatives from 1 H-indol-3-acetohydrazide, J. Struct. Chem. 54 (2013) 148–154.
[13] G. Ferguson, C. Glidewell, J.N. Low, J.M.S. Skakle, J.L. Wardell, Three isomeric (E)-nitrobenzaldehyde nitrophenylhydrazones: chains of rings in isomorphous (E)-2-nitrobenzaldehyde 3-nitrophenylhydrazone and (E)-3-nitrobenzaldehyde 2-nitrophenylhydrazone, and centrosymmetric dimers in (E)-4-nitrobenzaldehyde 2-nitrophen, Acta Crystallogr. Sect. C Cryst. Struct. Commun. 61 (2005) o613–o616.
[14] T.C. Baddeley, R.A. Howie, C.H. da Silva Lima, C.R. Kaiser, M.V.N. de Souza, J.L. Wardell, S.M.S.V Wardell, Pyrazinecarbonyl) hydrazone halobenzaldehydes: supramolecular arrays generated by face to face stacking of ribbons, formed from C–H–O interactions (2009).
[15] M.U. Ahmad, M. Rafiq, B. Zahra, M. Islam, M. Ashraf, M. al-Rashida, A. Khan, J. Hussain, Z. Shafiq, A. Al-Harrasi, Synthesis of benzimidazole based hydrazones as non-sugar based α-glucosidase inhibitors: structure activity relation and molecular docking, Drug. Dev. Res (2021), doi:10.1002/ddr.21807.
[16] M. Rafiq, M. Khalid, M.N. Tahir, M.U. Ahmad, M.U. Khan, M.M. Naseer, A.A.C. Braga, S. Muhammad, Synthesis, XRD, spectral (IR, UV–Vis, NMR) characterization and quantum chemical exploration of benzoimidazole-based hydrazones: a synergistic experimental-computational analysis, Appl. Organomet. Chem. 33 (2019) e5182.
[17] M. Khalid, M.N. Arshad, M.N. Tahir, A. M.Asiri, M.M. Naseer, M. Ishaq, M.U. Khan, Z. Shafiq, An efficient synthesis, structural (SC-XRD) and spectroscopic (FTIR, 1HNMR, MS spectroscopic) characterization of novel benzofuran-based hydrazones: an experimental and theoretical studies, J. Mol. Struct. 1216 (2020) 128318.
[18] Q-un-Nisa Tariq, S. Malik, A. Khan, M.M. Naseer, S.U. Khan, A. Ashraf, M. Ashraf, M. Rafiq, K. Mahmood, M.N. Tahir, Z. Shafiq, Xanthenone-based hy-

drazones as potent α-glucosidase inhibitors: synthesis, solid state self-assembly and in silico studies, Bioorg. Chem 84 (2019) 372–383.
[19] S. Naseem, M. Khalid, M.N. Tahir, M.A. Halim, A.A.C. Braga, M.M. Naseer, Z. Shafiq, Synthesis, structural, DFT studies, docking and antibacterial activity of a xanthene based hydrazone ligand, J. Mol. Struct. 1143 (2017) 235–244.
[20] M.U. Kumar, A.P. Jeyakumari, M. Suresh, S. Chandran, G. Vinitha, Synthesis, spectroscopic and DFT studies of Schiff based (E)-N′-(Benzo [d][1, 3] Dioxol-5-ylmethylene) nicotinohydrazide monohydrate single crystal: a promising organic nonlinear optical material, Mater. Res. Express. 6 (2019) 75102.
[21] D. Cheshmedzhieva, P. Ivanova, S. Stoyanov, D. Tasheva, M. Dimitrova, I. Ivanov, S. Ilieva, Experimental and theoretical study on the absorption and fluorescence properties of substituted aryl hydrazones of 1, 8-naphthalimide, Phys. Chem. Chem. Phys. 13 (2011) 18530–18538.
[22] J. Jia, Y. Li, J. Gao, A series of novel ferrocenyl derivatives: schiff bases-like push-pull systems with large third-order optical responses, Dye. Pigment. 137 (2017) 342–351.
[23] M. Shankar, A.D. Raj, M. Jeeva, R. Purusothaman, M. Vimalan, I.V. Potheher, Synthesis, crystal growth, thermal and laser damage threshold properties of new Schiff base NLO material 4-Nitro-benzoic acid (3-ethoxy-2-hydroxy-benzylidene)-hydrazide, Mater. Lett. 232 (2018) 113–117.
[24] D.-S. Yang, E)-4-Chloro-N′-(4-hydroxybenzylidene) benzohydrazide, Acta Crystallogr. Sect. E Struct. Reports Online. 64 (2008) o1849–o1849.
[25] G.A. El-Hiti, B.F. Abdel-Wahab, M.A. Baashen, E. Yousif, A.S. Hegazy, B.M. Kariuki, 2-(Naphthalen-2-yloxy)-N′-[2-(naphthalen-2-yloxy) acetyl] acetohydrazide monohydrate, IUCrData 6 (2021) x210314.
[26] Q. Chai, Y. Zhang, C.H. Liu, Mycobacterium tuberculosis: an adaptable pathogen associated with multiple human diseases, Front. Cell. Infect. Microbiol. 8 (2018) 158, doi:10.3389/FCIMB.2018.00158/BIBTEX.
[27] S.R. Luckner, N. Liu, C.W. Am Ende, P.J. Tonge, C. Kisker, A slow, tight binding inhibitor of InhA, the enoyl-acyl carrier protein reductase from Mycobacterium tuberculosis, J. Biol. Chem. 285 (2010) 14330–14337, doi:10.1074/JBC.M109.090373.
[28] G.M. Sheldrick, SHELX-97, University of Göttingen: Göttingen, Germany, 1997.
[29] M.J. Frisch, G.W. Trucks, H.B. Schlegel, G.E. Scuseria, M.A. Robb, J.R. Cheeseman, G. Scalmani, V. Barone, B. Mennucci, G.A. Petersson, in: Gaussian 09, 32, Gaussian, Inc, Wallingford, CT, 2009, pp. 5648–5652.
[30] R. Dennington, T. Keith, J. Millam, GaussView 5 (2009) Version.
[31] M.H. Jomroz, 'Vibrational energy distribution analysis VEDA4 (Warsaw), (2004).
[32] N.Q. Shikhaliyev, K.N. Bagirova, A.A. Niyazova, G.Z. Mammadova, J. Cisterna, A. Cárdenas, I. Brito, Crystal structure and hirshfeld surface analysis of (E)-1-(4-Bromophenyl)-2-(2, 2-Dichloro-1-(4-Fluorophenyl) vinyl) diazene, Crystallogr. Rep. 65 (2020) 1169–1172.
[33] K.T.A. AIMAll, in: TK Gristmill Software, Overland Park, KS, USA, 2019, p. 12. Version. 19 (n.d.
[34] C. Lu, C. Wu, D. Ghoreishi, W. Chen, L. Wang, W. Damm, G.A. Ross, M.K. Dahlgren, E. Russell, C.D. Von Bargen, R. Abel, R.A. Friesner, E.D. Harder, OPLS4: improving force field accuracy on challenging regimes of chemical space, J. Chem. Theory Comput. 17 (2021) 4291–4300 doi:10.1021/ACS.JCTC.1C00302/SUPPL_FILE/CT1C00302_SI_002.ZIP.
[35] H.M. Berman, T. Battistuz, T.N. Bhat, W.F. Bluhm, P.E. Bourne, K. Burkhardt, Z. Feng, G.L. Gilliland, L. Iype, S. Jain, P. Fagan, J. Marvin, D. Padilla, V. Ravichandran, B. Schneider, N. Thanki, H. Weissig, J.D. Westbrook, C. Zardecki, The protein data bank, Acta Crystallogr. Sect. D Biol. Crystallogr. 58 (2002) 899–907, doi:10.1107/S0907444902003451.
[36] J.C. Shelley, Æ.A. Cholleti, Æ.L.L. Frye, J.R. Greenwood, Æ.M.R. Timlin, Epik : a software program for pK a prediction and protonation state generation for drug-like molecules, (2007) 681–691. doi:10.1007/s10822-007-9133-z.
[37] Schrödinger, LigPrep 1 (2020).
[38] W. Sherman, T. Day, M.P. Jacobson, R.A. Friesner, R. Farid, Novel procedure for modeling ligand/receptor induced fit effects, J. Med. Chem. (2006), doi:10.1021/jm050540c.
[39] J. Rakovan, Computer programs for drawing crystal shapes and atomic structures, Rocks Miner 93 (2018) 60–64.
[40] L.J. Farrugia, WinGX and ORTEP for Windows: an update, J. Appl. Crystallogr. (2012), doi:10.1107/S0021889812029111.
[41] A. Gavezzotti, Efficient computer modeling of organic materials. The atom–atom, Coulomb–London–Pauli (AA-CLP) model for intermolecular electrostatic-polarization, dispersion and repulsion energies, New J. Chem. 35 (2011) 1360–1368.
[42] E. Espinosa, I. Alkorta, J. Elguero, E. Molins, From weak to strong interactions: a comprehensive analysis of the topological and energetic properties of the electron density distribution involving X–H··· F–Y systems, J. Chem. Phys. 117 (2002) 5529–5542.
[43] T.A. Nibila, T.K.S. Ahamed, P.P. Soufeena, K. Muraleedharan, P. Periyat, K.K. Aravindakshan, Synthesis, structural characterization, Hirshfeld surface and DFT based reactivity, UV filter and NLO studies of Schiff base analogue of 4-aminoantipyrine, Results Chem 2 (2020) 100062.
[44] R. Mani, I.B. Rietveld, B. Nicolaï, K. Varadharajan, M. Louhi-Kultanen, S. Narasimhan, Fluorescence and physical properties of the organic salt 2-chloro-4-nitrobenzoate–3-ammonium-phenol, Chem. Phys. 458 (2015) 52–61.
[45] N. Latha, D. Barathi, M. Uthaya Kumar, K.N. Vennila, G. Vinitha, R. Mani, M. Louhi-Kultanen, F. Bardak, A. Atac, E. Kose, Structural, theoretical and third order nonlinear optical properties of (E)-N'-(4-chlorobenzylidene)-4-fluorobenzohydrazide monohydrate, Mol. Cryst. Liq. Cryst. (2021) 1–15.
[46] V. Krishnakumar, M. Rajaboopathi, R. Nagalakshmi, Studies on vibrational, dielectric, mechanical and thermal properties of organic nonlinear optical co-crystal: 2, 6-diaminopyridinium–4-nitrophenolate–4-nitrophenol, Phys. B Condens. Matter. 407 (2012) 1119–1123.
[47] V. Choudhary, A. Bhatt, D. Dash, N. Sharma, DFT calculations on molecular structures, HOMO–LUMO study, reactivity descriptors and spectral analyses of newly synthesized diorganotin (IV) 2-chloridophenylacetohydroxamate complexes, J. Comput. Chem. 40 (2019) 2354–2363.
[48] M. Rana, N. Singla, A. Chatterjee, A. Shukla, P. Chowdhury, Investigation of nonlinear optical (NLO) properties by charge transfer contributions of amine functionalized tetraphenylethylene, Opt. Mater. (Amst). 62 (2016) 80–89.
[49] S.R. Marder, J.E. Sohn, G.D. Stucky, Materials For Nonlinear Optics Chemical Perspectives, American Chemical Society, Washington DC, 1991.
[50] M. Hurtta, I. Pitkänen, J. Knuutinen, Melting behaviour of D-sucrose, D-glucose and D-fructose, Carbohydr. Res. 339 (2004) 2267–2273.
[51] Y. Dong, R. Fan, W. Chen, P. Wang, Y. Yang, A simple quinolone Schiff-base containing CHEF based fluorescence 'turn-on'chemosensor for distinguishing Zn 2+ and Hg 2+ with high sensitivity, selectivity and reversibility, Dalt. Trans. 46 (2017) 6769–6775.
[52] R. Mekala, R. Mani, I.B. Rietveld, P. Jagdish, R. Mathammal, H. Jiang, Crystal growth and physical properties of the organic salt benzimidazolium 3-nitrophthalate, CrystEngComm 18 (2016) 8194–8206.
[53] M. Uthayakumar, A.P. Jeyakumari, G. Anbalagan, J.S. Kumar, T.S.R. Devi, Synthesis, crystal structure, spectroscopic, DFT computations and third-order nonlinear optical studies of Schiff-based (E)-N′-(benzo[*d*][1,3]dioxol-5-ylmethylene)-4-methoxybezohydrazide monohydrate single crystal, Appl. Phys. A Mater. Sci. Process. 125 (2019) 1–13, doi:10.1007/s00339-019-3008-8.
[54] F.Z. Henari, P.S. Patil, Nonlinear optical properties and optical limiting measurements of {(1Z)-[4-(Dimethylamino) Phenyl] Methylene} 4-Nitrobenzocarboxy Hydrazone Monohydrate under cw laser regime, Opt. Photonics J. 2014 (2014).
[55] H. Purandara, S. Raghavendra, S. Foro, P. Patil, B.T. Gowda, S.M. Dharmaprakash, P. Vishwanatha, Synthesis, spectroscopic characterization, crystal structure, Hirshfeld surface analysis and third-order nonlinear optical properties of 2-(4-chlorophenoxy)-N'-[(1E)-1-(4-methylphenyl) ethylidene] acetohydrazide, J. Mol. Struct. 1185 (2019) 205–211.